Charles University in Prague

Faculty of Science

DOCTORAL THESIS

RNDr. Anton Repko

Příprava magnetických nanočástic hydrotermální metodou

Preparation of magnetic nanoparticles by hydrothermal method

Department of Inorganic Chemistry

Supervisor of the doctoral thesis: Daniel Nižňanský

Study program: Inorganic Chemistry

Prague, 2014

I would like to thank Daniel Nižňanský for support during the experimental work, and Jana Vejpravová for magnetic measurements and their explanation. I also appreciate the time spent by Jaroslav Kupčík and Carla Cannas (among others) doing transmission electron microscopy, even when the results were not suitable for publication.

Prohlášení:
Prohlašuji, že jsem závěrečnou práci zpracoval samostatně a že jsem uvedl všechny použité informační zdroje a literaturu. Tato práce ani její podstatná část nebyla předložena k získání jiného nebo stejného akademického titulu.

I declare that I carried out this doctoral thesis independently, and I cited all information sources and literature. Neither this work nor its essential part was proposed with aim to obtain another or the same academic degree.

In Prague, date 11.7.2014

Název práce: Příprava magnetických nanočástic hydrotermální metodou

Autor: RNDr. Anton Repko

Katedra: Katedra anorganické chemie, PřF UK Praha

Vedoucí disertační práce: RNDr. Daniel Nižňanský, PhD

Abstrakt:

Hydrotermální metodě přípravy nanočástic s využitím kyseliny olejové byla v posledních letech věnována jistá pozornost, nicméně publikované práce trpí nedostatkem systematického přístupu a mechanismus nebyl přezkoumán natolik, aby byly dosaženy předvídatelné výsledky syntéz. V předkládané práci byl zkoumán vliv složení organické a vodní fáze na syntézu nanočástic feritu kobaltnatého (oxidu kobaltnato-železitého) a magnetitu, přičemž byl navržen mechanizmus tvorby částic. Organická fáze se skládala z pentanolu, oktanolu nebo toluenu, s obsahem prekurzoru – oleátu prvků skupiny železa. Kromě hydrofobních částic bylo možno dokonce přímo připravit hydrofilní částice pokryté oleátem, a to s využitím vodní fáze obsahující oleát sodný. Syntetický postup byl dále zjednodušen oddělenou přípravou oleátu kobaltnato-železitého, čímž byl získán produkt s užší distribucí velikostí a lepší fázovou čistotou. Byla dosažena kontrola velikosti v rozsahu 6–11 nm, s výtěžkem cca. 500 mg na syntézu.

Pozornost byla věnována také povrchové úpravě, vedoucí k hydrofilním částicím. Byly použity di- a trikarboxylové kyseliny s krátkým řetězcem a také karboxymethyl-dextran a oxid titaničitý. Oxid titaničitý vyžadoval dodatečnou ochranu kyselinou nitrilotris(methylfosfonovou) za účelem stabilizace produktu ve vodní disperzi.

Ke kontrole fázové čistoty a pro určení velikosti částic byla použita prášková rentgenová difrakce. Připravené částice byly charakterizovány také transmisní elektronovou mikroskopií, dynamickým rozptylem světla, Mössbauerovou spektroskopií a magnetickými měřeními na SQUIDu, konkrétně měřením zero-field-cooled a field-cooled magnetizace, hysterezních smyček a střídavé susceptibility.

Předkládaná práce obsahuje také detailnější vysvětlení analýzy rentgenové difrakce a Mössbauerovy spektroskopie. Ostatní metody charakterizace jsou dostatečně diskutovány v přiložených publikacích.

Klíčová slova: ferit kobaltnatý, nanokrystaly, modifikace povrchu, superparamagnetismus, kyselina olejová

Title: Preparation of magnetic nanoparticles by hydrothermal method

Author: RNDr. Anton Repko

Department: Department od Inorganic Chemistry, Faculty of Science, Charles University in Prague

Supervisor: RNDr. Daniel Nižňanský, PhD

Abstract:

Hydrothermal method of nanoparticle preparation, involving oleic acid, has received certain attention in the last years. However, the published works lack systematic approach to the subject, and the mechanism was not thoroughly investigated, so as to achieve a predictable outcome of the synthesis. The present work investigated the influence of composition of organic and water phase on the synthesis of cobalt ferrite (cobalt(II)-iron(III) oxide) and magnetite nanoparticles, and the mechanism of nanoparticle formation was proposed. Organic phase was based on pentanol, octanol or toluene, containing the precursor – metal oleate. Besides hydrophobic particles, it was even possible to directly prepare hydrophilic oleate-coated particles by using water phase with sodium oleate. Synthetic procedure was then simplified by a separate preparation of cobalt-iron oleate, which led also to a product of narrower size distribution and better phase purity. Size control in the range of 6–11 nm and a batch yield of ca. 500 mg was achieved.

Attention was given also to the surface modification of the particles, thus imparting them hydrophilicity. Small di- or tricarboxylic acids were utilized, as well as carboxylmethyl dextran and titanium dioxide. Titanium dioxide required additional protection with nitrilotri(methylphosphonic acid) to stabilize the product in water dispersion.

Powder X-ray diffraction (XRD) was used to check the phase purity and to estimate the particle size. Prepared particles were characterized also by transmission electron microscopy, dynamic light scattering, Mössbauer spectroscopy and magnetic measurements on SQUID by means of zero-field-cooled and field-cooled magnetizations, hysteresis loops, and alternating-current (AC) susceptibility.

The present thesis also provides a more detailed explanation of XRD analysis and Mössbauer spectroscopy. Remaining characterization methods are sufficiently discussed in the attached publications.

Keywords: cobalt ferrite, nanocrystals, surface modification, superparamagnetism, oleic acid

Contents

1. Introduction

Magnetic nanoparticles are a widely studied material due to their various potential applications and interesting physical properties, namely superparamagnetism, which is characteristic by disappearance of coercivity in otherwise ferro- or ferrimagnetic materials. Small size and magnetic properties are interesting not only from purely physical point of view, but are favorable also in biomedical area which currently attracts large attention [1]. Magnetite (Fe_3O_4) is the material of choice due to its low toxicity. Besides magnetite, the present thesis focuses mainly on cobalt ferrite ($CoFe_2O_4$) due to its better chemical stability and high coercitive field (2 Tesla at 10 K, compared to ca. 20 mT for magnetite). Both compounds crystallize in a spinel structure AB_2O_4, where oxygen occupy face-centered cubic lattice, ions $A^{2/3+}$ are located in tetrahedral and $B^{2/3+}$ in octahedral positions. Medical applications of these materials were not directly addressed, since the aim was on synthesis and evaluation of physical properties, although certain considerations were taken into account during the development of surface modifications.

The thesis is organized as follows: First, superparamagnetism is briefly discussed, followed by a literature review on applications and synthesis of nanoparticles. Then, a somewhat deeper mathematical description of XRD evaluation and Mössbauer spectroscopy is given. Next chapter discusses preparation of the nanoparticles from a chemical point of view. Their characterization is presented in the attached articles [A1–3] which are the integral part of the thesis. The product of the best quality is described in [A3], mainly from the magnetic point of view. Some additional characterizations, such as dynamic light scattering, zeta potential measurement and infrared spectroscopy are given in [A1] and [A2].

1.1 Superparamagnetism

Magnetic materials, when their crystal size is decreased under the typical domain size, give rise to monodomain (nano)particles, and have been a subject of intensive research in recent years [2, 3]. If the magnetocrystalline anisotropy is sufficiently high and the thermal energy is unable to overcome it, the magnetic moment of the whole particle remains frozen in the easy axis of magnetization, and the particle is in the so-called blocked state. By decreasing the size of the particle, or by exceeding the so-called *blocking temperature*, the particle becomes superparamagnetic, its magnetic moment (so-called *superspin*) is randomly flipping, and the coercivity (H_c) is zero. Fig. 1.1 shows typical hysteresis loops (magnetization isotherms) obtained by cycling the dried sample of nanoparticles in external field of -7 T to 7 T at low and room temperature, and measuring the magnetization by SQUID magnetometer.

The reason of high coercivity (2 T) of $CoFe_2O_4$ is the magnetocrystalline anisotropy caused by the spin-orbital coupling in Co^{2+}. Cubic spinel structure of $CoFe_2O_4$ has its easy axes along the cube edges and the anisotropy energy (per unit volume) in arbitrary direction can be expressed as

$$E/V = E_0/V + K_1(\alpha_1^2\alpha_2^2 + \alpha_2^2\alpha_3^2 + \alpha_3^2\alpha_1^2) + K_2(\alpha_1^2\alpha_2^2\alpha_3^2) + \dots \qquad (1.1)$$

where K_1 and K_2 are known as the first and second anisotropy constants, and

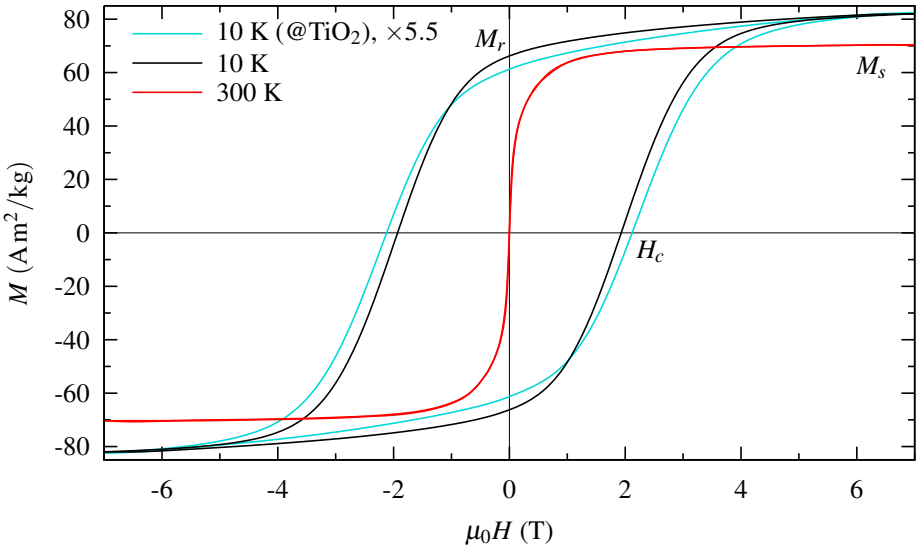

Figure 1.1: Hysteresis loops of citrate-coated (almost bare) and TiO_2-coated (diluted) 10.5 nm particles of $CoFe_2O_4$ [A3] in their blocked ($T = 10$ K) and superparamagnetic ($T = 300$ K) state, showing coercitive field H_c, remanent magnetization M_r and saturated magnetization M_s. The differences in H_c and M_r/M_s for dense and diluted samples point to a different interplay of magnetocrystalline anisotropy and inter-particle interactions in both cases.

α_1, α_2, α_3 are direction cosines with respect to cube edges [4]. The path of easiest flipping from one easy axis to another goes through the center of cube edge, so the activation energy of the superspin flipping is related to a direction along face diagonal, where $\alpha_1 = \alpha_2 = \cos(\pi/4) = \sqrt{1/2}$ and $\alpha_3 = 0$:

$$E_a = \tfrac{1}{4} K_1 V = K_{\text{eff}} V \tag{1.2}$$

Another type of anisotropy is the axial one, with much simpler angular dependence of energy,

$$E = K_1 V \sin^2 \theta, \tag{1.3}$$

and is therefore a preferred subject of modelling of the magnetization dynamics in nanoparticles [5]. Axial anisotropy is also often of the shape origin, where the easy axis (along the prolongation) is implied by the demagnetization field, which can be illustrated by the properties of aligned dipolar magnets: they attract in a head-to-tail arrangement, but repel when placed side-by-side.

The magnetization anisotropy is the main factor which causes freezing of the superspin at low temperatures. Transition to superparamagnetic state is then given by thermal energy, which leads to decreasing relaxation time τ of the superspin as rising $k_B T$ approaches the anisotropy-related activation energy E_a. In the first approximation, the relaxation time is given by the Néel-Arrhenius relation [5]

$$\tau = \tau_0 \exp \frac{E_a}{k_B T}, \tag{1.4}$$

but a more precise treatment should include also the temperature dependence of inverse attempt frequency τ_0 [5] and even of magnetocrystalline anisotropy [4].

The most useful method for evaluation of the blocking temperature (i.e. of the transition between superparamagnetic and blocked state) in a time scale of $\tau \approx 10^3$ s is the measurement of zero-field-cooled and field-cooled magnetization [6]. A sample (usually ca. 10 mg of dried material) is cooled in zero external magnetic field to low temperature, then a small magnetic field is applied (e.g. 10 mT), and the sample is gradually heated while measuring its magnetization, thus obtaining the ZFC curve. The sample is then again cooled, keeping the external field, and the FC curve is recorded. An example of ZFC/FC measurement for 6 nm $CoFe_2O_4$ particles is given in Fig. 1.2. The maximum of ZFC curve is interpreted here as the blocking temperature T_B. As can be seen in Fig. 1.2, the ZFC and FC curves overlap for higher temperatures, indicating independence of magnetization on its history, which is a clear demonstration of the superparamagnetic state.

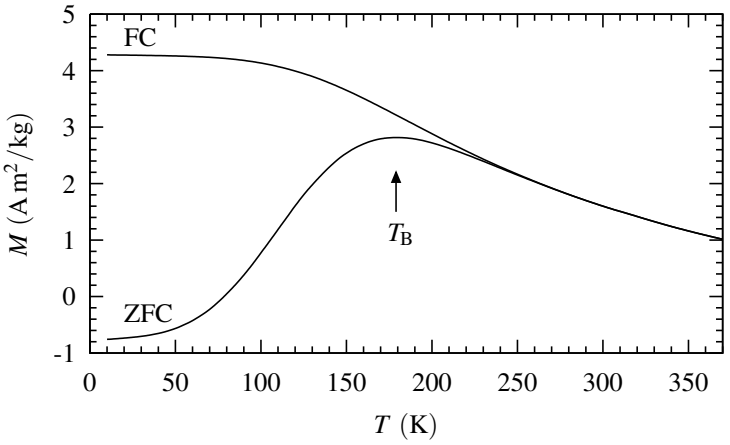

Figure 1.2: Zero-field-cooled and field-cooled magnetization of a dried sample of 6 nm oleate-coated $CoFe_2O_4$ [A3].

A shorter time scale ($10^1 - 10^{-3}$ s) is achieved in the measurement of alternating-current (AC) susceptibility, where an analog of the blocking temperature can be obtained as the temperature T_f at the maximum of real susceptibility χ' (see [A3]). Mössbauer spectroscopy (see section 3.2) then gives some information about superspin relaxation in the region of 10^{-7} s.

The previous discussion did not explicitly assume inter-particle interactions. These interactions can significantly influence the magnetic properties of the material, leading to higher apparent blocking temperature, which is in fact a freezing temperature of intrinsically superparamagnetic particles, whose superspin rotation is suppressed due to inter-particle interactions, usually of dipolar origin. Such shifting of the blocking temperature was demonstrated in [A3]. To describe these interactions quantitatively, frequency dependence of AC susceptibility is usually analyzed, where the frequency gives explicitly the time scale: $\tau = 1/f$. Two approaches were utilized to describe the frequency dependence of T_f, namely the Vögel-Fulcher law [7, 8]

$$\tau = \tau_0 \exp \frac{K_{\text{eff}} V}{k_B (T - T_0)} \qquad \text{with } \tau_0 \approx 10^{-9} - 10^{-12} \text{ s}, \tag{1.5}$$

which has a form similar to Néel-Arrhenius law (1.4), supplemented by a temperature T_0, which is a measure of inter-particle interactions. Second approach is

based on the description of critical behavior near a phase transition, and assumes a power law [9]

$$\tau = \tau^* \left(\frac{T}{T - T^*} \right)^{z\nu} \tag{1.6}$$

with critical exponent $z\nu$ in the range $5 - 11$. Both these laws were at first proposed for spin glasses, where magnetic atoms (Mn or Fe) are diluted in inert matrix, which leads to a random distribution of magnetic interactions. These approaches were later applied also to *superspin glasses*, where the atomic spins are replaced by superparamagnetic particles [3].

There are also other ways to describe inter-particle interactions, namely the interacting superparamagnet model, analyzing the magnetization isotherms [10], and Cole-Cole plots of imaginary (χ'') vs. real (χ') AC susceptibility [11]. These approaches were not employed in our work.

2. Literature review

The following sections review the synthetic approaches to magnetic nanoparticles, prepared with the aim of dispersibility in water or organic medium. There are also various widely-applied solid-state methods of preparation of nanocrystalline magnetic materials, such as ball-milling, citrate combustion, sol-gel annealing, laser pyrolysis etc, which are not treated here, since they are out of scope of the present work.

2.1 Applications

Probably the most extensive application area now is medicine, where the magnetic particles can be used in various ways: either for drug delivery (chemotherapy, gene delivery, magnetically guided photodynamic therapy, etc.), or for hyperthermical treatment of tumors (via application of alternating magnetic field), as a contrast agent in magnetic resonance imaging, for cell labeling, etc [1]. All these works employ magnetite (Fe_3O_4) or maghemite (γ-Fe_2O_3, the product of spontaneous oxidation of magnetite) due to their biocompatibility and degradability.

Other applications include catalysis, either directly [12, 13], or as a carrier for magnetically separable catalysts, e.g. TiO_2 [14, 15]. $CoFe_2O_4$ nanoparticles can be used also for magnetic recording, but they have to be large enough (18 nm) to be in blocked ferrimagnetic state. Nevertheless, they do not reach the memory density of currently utilized materials [16].

2.2 Direct preparation of hydrophilic particles

The most simple way of preparation of ferrite nanoparticles is the coprecipitation of iron salts with ammonia. To get stable water dispersion for biomedical application, usually a surfactant, e.g. dextran, is introduced into precursor solution [17].

Better monodispersity and lower aggregation can be achieved by microemulsion method, where the growing particles are physically separated by micelles of oil-in-water [18, 19] or reverse micelles of water-in-oil [20] and a wide size range (5 – 30 nm) can be achieved [21, 22]. There remains a disadvantage of lower batch yield and lower crystallinity of the product, although these drawback can be somewhat circumvented by carrying out synthesis at higher temperature (90 °C) [23].

Even higher reaction temperature (160 °C) can be achieved by refluxing in polyol (1,2-propanediol), where hydrolysis of iron and cobalt salts by sodium acetate leads to 5 nm $CoFe_2O_4$ particles [24]. The cited work is an example of spontaneous hydrolysis of metal carboxylates at increased temperature (which are otherwise stable at room temperature) and the same principle is elaborated in the present thesis.

A common obstacle of all mentioned syntheses of hydrophilic particles is an unavoidable aggregation, which influences the physical properties due to strong magnetic inter-particle interactions. Therefore, the methods, which lead to hy-

drophobic particles coated with long chain molecules (and dispersible in hexane, toluene etc), are preferred for preparation of high-quality and well separated particles, and are described in the following sections.

2.3 Thermal decomposition in high-boiling organic solvents

The method, which is most widely utilized for preparation of high-quality and monodisperse hydrophobic particles of magnetite and ferrites, is the thermal decomposition of certain metallic precursors in high-boiling organic solvents, usually in the presence of oleic acid and/or oleylamine. For example, MFe_2O_4 nanoparticles can be prepared by refluxing Fe/Co/Mn acetylacetonates in diphenylether or dibenzylether in the presence of oleic acid, oleylamine and 1,2-hexadecanediol [25]. Multi-gram yields of magnetite were reported for decomposition of iron(III) oleate in 1-octadecene and similar solvents [26], and analogously for cobalt ferrite [27].

Although the thermal decomposition became almost standard in the field of preparation of monodisperse nanoparticles, its practical realization often encounters various obstacles. First, removal of the solvents from the product tends to be difficult, mainly in the case of octadecene, and although solvent-free procedures were proposed [28], these often suffer from broader size distribution. Then, reproducibility can be seriously affected by necessity of keeping the given heating rate [27], by the age of cobalt-iron oleate [29], or by the prior amide formation between oleic acid and oleylamine [30].

2.4 Hydrothermal method with fatty acid

Hydrophobic particles coated with a layer of fatty acid, as described in the previous section, have an advantage of low aggregation, and can be prepared also in systems where water is present. The reaction vessel needs to be hermetically sealed to sustain increased pressure. However, stirring is usually not applied, so the size distribution is mostly broader than for thermal decomposition. One of the first reports proposed a usage of linoleic acid, sodium linoleate and corresponding metal salt in a mixed solvent of ethanol and water, to obtain a wide range of nanoparticulate materials [31]. Subsequent reports then usually shifted to oleic acid, preparing iron oxides [32], $CoFe_2O_4$ [33], (Cd,Zn)Se [34], LaF_3 [35], $Na(Y,Gd)F_4$ [36]. The usually proposed mechanism is based on a three phase system, so-called liquid-solid-solution (LSS) phase transfer. The phases in question are fatty acid, sodium oleate (or linoleate) and water + ethanol. Since the metal ions react with oleic anions, sodium oleate has to be present in large excess to preserve the intended solid phase. Therefore, the amount of metal ions is comparatively low, and batch yields are around 100 mg, which is the possible reason, why the method was not so widely employed, as was seen for thermal decomposition.

As I show later, the presence of free sodium oleate is not necessary at all, and this fact enables to increase the batch yield. However, it is necessary to replace ethanol with higher alcohol or toluene, to achieve acceptable uniformity of the

particles [A1]. The replacement of ethanol by a less polar solvent was employed also by other authors, however, their methods usualy deviate from the original concept to a larger extent. Tian [37] utilized $Fe(acac)_3$ in a mixture of octanol and oleylamine (no free water was present). Baruwati [38] took the product of coprecipitation (from metal nitrates and ammonia) and treated it hydrothermally with a mixture of toluene and oleic acid. Toluene was also used by Feng [13] to dissolve the metal oleates formed by the reaction with sodium oleate, however, he also added tert-butylamine before the hydrothermal treatment. It appears that the authors a priori add some alkaline reagents, as if formation of oxide particles required forced hydrolysis. The present thesis shows that this presumption is not necessary, and the hydrolysis of cobalt and iron oleates occurs spontaneously in the hydrothermal conditions, as is most explicitly shown in the last part of my work [A3].

2.5 Surface modification

Although nanoparticles from thermal decomposition or hydrothermal method are well dispersed, stable and well suited for physical characterization, there is often a need to transform them to a hydrophilic state. This aim is frequently achieved by coating with silanes [39] and/or SiO_2 [40].

The stability of oleate-coated particles points to a large affinity of carboxylic group to the surface of ferrite nanoparticles. It is therefore desirable to replace oleic acid with other, preferentially di- or tri-carboxylic acid, to yield hydrophilic particles. This modification can be done in toluene + dimethylsulfoxide, where the hydrophobic particles and modifying acid are both dispersed/dissolved. 2,3-dimercaptosuccinic acid (DMSA) [41] is well suited for this purpose, as it provides SH functionality for further coupling. On a small scale (10 mg), the ligand exchange can be reportedly done also by spontaneous phase transfer of particles from organic phase to water phase containing citrate [42].

Coating with polymers, which is a common type of modification for already-hydrophilic particles, turns out to be somewhat non-trivial for oleate coated particles, due to their hydrophobic nature. Therefore, multi-step procedures are usually employed, e.g. polyethylene glycol (PEG) and carboxymethyl-dextran were attached to the magnetite nanoparticles through amide coupling to 3-aminopropylsilane-modified particles [43], and PEG-diamine was attached to DMSA-modified particles [44]. My work [A2] descibes another approach, which involves direct modification of oleate-coated, but hydrophilic particles with carboxymethyl dextran.

3. Characterization methods

3.1 Powder X-ray diffraction and particle size distribution

The size of the nanocrystals was analyzed not only by the electron microscopy, but also by fitting the X-ray diffraction profile. Before derivation of the needed formula of the Scherrer type, the basic principles of diffraction will be briefly reviewed, mainly to define reciprocal space, in which the fitting was done.

3.1.1 Reciprocal lattice

The X-ray diffraction can be thought of as an elastic scattering of high energy photons on a periodic electron density of a crystal lattice. Scattering event can be characterized by a vector $\vec{q}$

$$\vec{q} = \frac{\vec{k}' - \vec{k}}{2\pi} = \frac{\vec{s}' - \vec{s}}{\lambda} \qquad q = |\vec{q}| = \frac{2\sin\theta}{\lambda} \tag{3.1}$$

where $\vec{k}$ and $\vec{k}'$ are wave vectors of incoming and scattered wave, $\vec{s}$ and $\vec{s}'$ are corresponding unit vectors in their direction, λ is wavelength, and θ is a scattering angle, as described in Fig. 3.1.

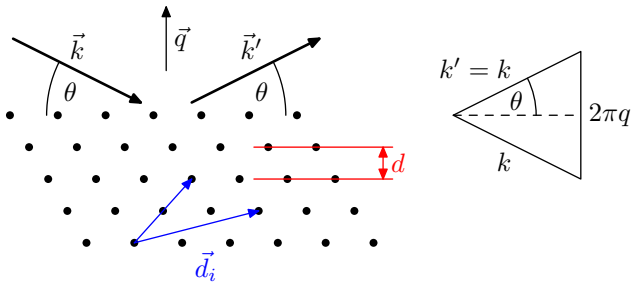

Figure 3.1: The geometry of diffraction on a crystal lattice. Direction of incoming and diffracted X-rays is indicated by their wave vectors, $\vec{k}$ and $\vec{k}'$. The triangle shows how to calculate the size of vector $\vec{q}$. Blue vectors ($\vec{d}_i$) give examples of translation symmetry.

The vector $\vec{q}$ can be related to the spatial distribution of electron density $\rho(\vec{r})$ through Fourier transformation, since the electric field intensity of the scattered wave, characterized by the vector $\vec{q}$, is proportional to the Fourier transformed electron density[1]

$$E(\vec{q}) \sim \int \rho(\vec{r}) \mathrm{e}^{-2\pi \mathrm{i} \vec{q}\cdot\vec{r}} \mathrm{d}\vec{r} \tag{3.2}$$

For infinite periodic lattice, where $\rho(\vec{r}) = \rho(\vec{r} + \vec{d}_i)$, with $\vec{d}_i$ being any translation vector from the symmetry group, the integral (3.2) is non-zero only when the

[1] The formula can be derived by tracing the incoming and scattered X-rays, using $E = E_0 \mathrm{e}^{\mathrm{i}\vec{k}\cdot\vec{r}}$ and (3.1)

Laue's conditions are satisfied for all $\vec{d}_i$

$$\vec{d}_i \cdot \vec{q} = integer \qquad \rightarrow \qquad q = \frac{n}{d} \tag{3.3}$$

where inter-planar distance d was conveniently defined as a projection of the translation vector $\vec{d}_i$ to the direction of vector $\vec{q}$ (or, to be more precise, the least common divisor of such projected translation vectors), and n is an integer dependent on the given $\vec{q}$. Equations (3.1) and (3.3) give together the familiar Bragg equation

$$n\lambda = 2d \sin\theta \tag{3.4}$$

The vectors $\vec{q}$ satisfying (3.3) can be conveniently classified by introducing *reciprocal lattice* with basis vectors $\vec{a}^*, \vec{b}^*, \vec{c}^*$, which is related to the (spatial) crystal lattice with basis vectors $\vec{a}, \vec{b}, \vec{c}$:

$$\begin{array}{l} \vec{r} = x\vec{a} + y\vec{b} + z\vec{c} \\ \vec{q} = h\vec{a}^* + k\vec{b}^* + l\vec{c}^* \end{array} \qquad \begin{array}{lll} \vec{a}\cdot\vec{a}^* = 1 & \vec{b}\cdot\vec{a}^* = 0 & \vec{c}\cdot\vec{a}^* = 0 \\ \vec{a}\cdot\vec{b}^* = 0 & \vec{b}\cdot\vec{b}^* = 1 & \vec{c}\cdot\vec{b}^* = 0 \\ \vec{a}\cdot\vec{c}^* = 0 & \vec{b}\cdot\vec{c}^* = 0 & \vec{c}\cdot\vec{c}^* = 1 \end{array} \tag{3.5}$$

The lattice vectors $\vec{a}, \vec{b}, \vec{c}$ were chosen in such a way that the translation symmetry vectors $\vec{d}_i$ have integer coordinates (x, y, z).[2] For crystals with cubic symmetry and lattice parameter a, the reciprocal lattice is orthogonal and the size of vector $\vec{q}$ is simply

$$q = \frac{\sqrt{h^2 + k^2 + l^2}}{a} \qquad \text{(cubic)} \tag{3.6a}$$

Another common lattice is the hexagonal one, for which the corresponding formula is

$$q = \sqrt{\frac{4(h^2 + hk + k^2)}{3a^2} + \frac{l^2}{c^2}} \qquad \text{(hexagonal).} \tag{3.6b}$$

Formula (3.6b) can be derived from the basis vectors of spatial and reciprocal lattice, using (3.5):

$$\vec{a} = \begin{pmatrix} a \\ 0 \\ 0 \end{pmatrix}, \quad \vec{b} = \begin{pmatrix} -a/2 \\ \sqrt{3}\,a/2 \\ 0 \end{pmatrix}, \quad \vec{c} = \begin{pmatrix} 0 \\ 0 \\ c \end{pmatrix} \quad \rightarrow \quad \begin{array}{l} \vec{a}^* = (1/a, 1/\sqrt{3}\,a, 0) \\ \vec{b}^* = (0, 2/\sqrt{3}\,a, 0) \\ \vec{c}^* = (0, 0, 1/c) \end{array} \tag{3.7}$$

For clarity, these vectors are depicted in Fig. 3.2.

3.1.2 Diffraction broadening due to finite crystal size

When the crystal is infinitely large, its Fourier transformation (3.2) gives infinitely small points (with various intensities, known as structural factors), located at the integer positions of reciprocal lattice. In practice, the crystal has a finite size, and I will assume spherical shape in the following. This fact can be described as a multiplication of the electron density (of an infinite crystal) by a solid sphere – a function, which is one for $|\vec{r}| \leq R$, and zero for $|\vec{r}| > R$. Fourier transformation

[2] This statement is not entirely valid for body- or face-centered lattices, which are not treated here for simplicity. In short, centering leads to disappearance of certain points in the reciprocal lattice.

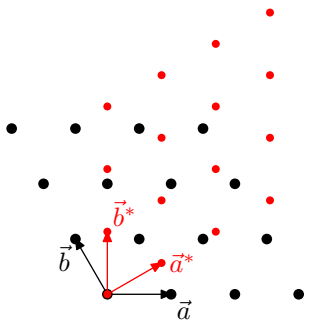

Figure 3.2: Spatial (black) and reciprocal (red) lattice for a hexagonal crystal. Placement and scaling of the reciprocal lattice is arbitrary, but the orientation is fixed.

then turns multiplication into convolution, so the points in the reciprocal lattice (i.e. vectors $\vec{q}$) will be smeared by a function, which is a Fourier transformation of the solid sphere. This function, here denoted as $f_R(q)$, is spherically symmetric, and the integral (3.2) will be evaluated in spherical coordinates:

$$\begin{aligned} f_R(q) &= \int_0^R \int_{-1}^1 \mathrm{e}^{-2\pi \mathrm{i} q r \cos\vartheta} 2\pi r^2 \,\mathrm{d}r \,\mathrm{d}\cos\vartheta = \int_0^R \frac{2\sin(2\pi q r)}{q} r \,\mathrm{d}r \\ &= \frac{1}{\pi q^2}\left(\frac{\sin(2\pi q R)}{2\pi q} - R\cos(2\pi q R)\right) \end{aligned} \tag{3.8}$$

The value $f_R(0)$ can be obtained using Taylor expansion:

$$f_R(0) = \lim_{q\to 0} \frac{1}{\pi q^2}\left(-\frac{4\pi^2 q^2 R^3}{3!} + \frac{4\pi^2 q^2 R^3}{2!} + O(q^4)\right) = \frac{4}{3}\pi R^3 \tag{3.9}$$

However, the diffraction intensity will be proportional to a square of the function $f_R(q)$. I will therefore define a normalized profile function $I_1(x)$, corresponding to the particles of unit diameter ($R = 1/2$)

$$I_1(x) = \left(\frac{f_{1/2}(x)}{f_{1/2}(0)}\right)^2 = \frac{9}{(\pi x)^6}[\sin(\pi x) - \pi x\cos(\pi x)]^2 \tag{3.10}$$

This function is plotted in Fig. 3.3 as the blue line. Its full width at half maximum (FWHM, or Γ) is 1.155, and it is narrower at the bottom than the Gauss function. However, when I assume an ensemble of spherical particles with log-normal size distribution around unit diameter (and weighted by particle volume), then the peak shape is modified, and acquires nearly Gaussian shape (with $\Gamma = 1.10$) for polydispersity $\sigma = 0.18$.

3.1.3 Log-normal distribution

Before continuing the discussion of X-ray diffraction, the log-normal distribution will be briefly reviewed. The normal (Gaussian) distribution

$$P_N(x, x_0, \sigma) = \frac{1}{\sqrt{2\pi}\,\sigma} \exp\left(-\frac{(x - x_0)^2}{2\sigma^2}\right) \tag{3.11}$$

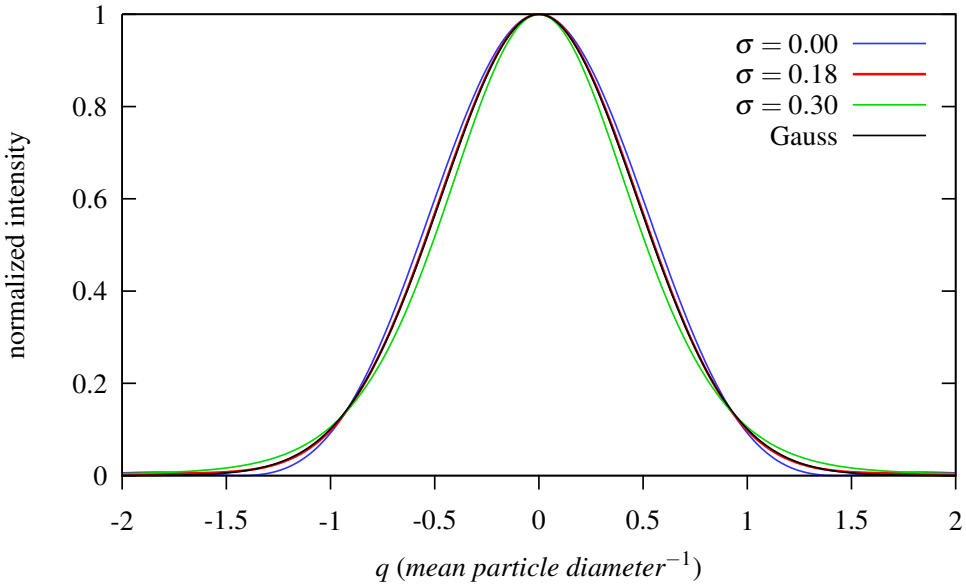

Figure 3.3: Calculated diffraction pattern (in reciprocal space) of the solid spheres with log-normal (volume weighted) size distribution with given polydispersity. Also the Gauss function with FWHM equal to 1.10 is plotted for comparison.

is natural for quantities involved in mutual addition or multiplication with a constant. This is not the case for particle size distribution. Rather, a log-normal distribution

$$P_{LN}(x, x_0, \sigma) = \frac{1}{\sqrt{2\pi}\,\sigma x} \exp\left(-\frac{(\ln x - \ln x_0)^2}{2\sigma^2}\right) \tag{3.12}$$

is better suited, because its character is kept when we shift our interest to e.g. particle volume, or volume-weighted distribution of particle size; only the parameters x_0 and σ are modified (shifted, scaled, etc.). The log-normal distribution is related to the normal one by a relation

$$P_{LN}(x, x_0, \sigma)\,\mathrm{d}x = P_N(\ln x, \ln x_0, \sigma)\,\mathrm{d}\ln x, \tag{3.13}$$

so the parameters $\ln x_0$ and σ can be obtained directly by usual statistical analysis of $\ln x$ as its mean and standard deviation. The log-normal distribution was used above (Fig. 3.3) to obtain the peak shape corresponding to the ensemble of spherical particles (with diameter D) by numerical evaluation of the expression

$$\frac{1}{N}\int P_{LN}(D, 1, \sigma) I_1(qD) D\,\mathrm{d}D, \tag{3.14}$$

where multiplication with D was introduced to keep a constant area of the scaled peak $I(qD)$, and the normalization constant N was chosen to keep unit height of the final peak.

3.1.4 Voigt function

When the particle distribution becomes more polydisperse, or other effects are included, the peak shape can become wider at its bottom part, approaching Lorentzian shape. To cover the range of shapes between Gaussian and Lorentzian,

the fitting of the XRD profile is conveniently done using Voigt function, which is a convolution of Gauss and Lorentz function. I will use the following prescription, explicitly giving Lorentzian (Γ_L) and Gaussian (Γ_G) partial FWHM, and approximately normalized to unit height.

$$V(q,\Gamma_G,\Gamma_L) = \frac{\Gamma_G+\Gamma_L}{\Gamma_G}\frac{\Gamma_L}{2\pi}\int\limits_{-\infty}^{+\infty}\frac{\exp\left(-\frac{z^2}{(\Gamma_G/2)^2}\ln 2\right)}{(q-z)^2+(\Gamma_L/2)^2}\mathrm{d}z \tag{3.15}$$

Voigt function has a property which is quite useful in XRD profile fitting, namely the easy subtraction of the instrumental broadening. I just need to assume Voigtian shape of both instrumental and sample's intrinsic profiles. Their full widths at half maximum will be denoted as Γ_G^{inst}, Γ_L^{inst}, and Γ_G, Γ_L, respectively. Measured profile is a convolution of both profiles, which is again a Voigt function, because convolution of two Lorentz functions gives another Lorentz function (its Fourier transform is $\exp(-\Gamma_L|x|/2)$, so the widths add), and convolution of two Gauss functions gives again a Gauss function (the widths add in square). The sample's intrinsic FWHMs are then obtained from measured ones (Γ_G^{meas}, Γ_L^{meas}) by

$$\Gamma_G^2 = (\Gamma_G^{\mathrm{meas}})^2 - (\Gamma_G^{\mathrm{inst}})^2 \qquad \Gamma_L = \Gamma_L^{\mathrm{meas}} - \Gamma_L^{\mathrm{inst}} \tag{3.16}$$

Finally, the total FWHM (Γ) of the (intrinsic) Voigt function can be calculated by the following approximation, with an inaccuracy of 0.02% [45]:

$$\Gamma = 0.5346\Gamma_L + \sqrt{0.2166\Gamma_L^2+\Gamma_G^2} \qquad \Gamma_G = \sqrt{(\Gamma+0.0692\Gamma_L)(\Gamma-\Gamma_L)} \tag{3.17}$$

The computation of Voigt function is numerically expensive, so I used an approximation implemented in `gnuplot`, with relative error less than 10^{-4} [46]. The `gnuplot` function $voigt(x,y)$ is related to definition (3.15) as follows:

$$voigt(x,y) = \frac{y}{\pi}\int\limits_{-\infty}^{+\infty}\frac{\exp(-t^2)}{(x-t)^2+y^2}\mathrm{d}t \tag{3.18}$$

$$V(x,\Gamma_G,\Gamma_L) = \frac{\Gamma_G+\Gamma_L}{\Gamma_G}\ voigt\left(\sqrt{\ln 2}\,\frac{2x}{\Gamma_G}, \sqrt{\ln 2}\,\frac{\Gamma_L}{\Gamma_G}\right) \tag{3.19}$$

3.1.5 Analysis of the diffraction profile. Scherrer equation

The diffraction profile is usually measured as a function of 2θ. As was explained at (3.8), the peak broadening is constant in reciprocal space (in variable q), so it is useful to construct the theoretical profile in q variable, using (3.1), and then we can constrain several peaks to have the same width. I will further re-parametrize Gaussian and Lorentzian widths using (3.17) and new variables Γ_i and x,

$$\Gamma_L = x\Gamma_i, \qquad \Gamma_G = \Gamma_i\sqrt{(1+0.0692x)(1-x)}, \tag{3.20}$$

where the index i labels the chosen diffraction. I use the same value of x for the whole spectrum to reduce the number of fitted parameters. The fitted profile is

then (with A_i being the amplitude)

$$I(2\theta) = \sum_i A_i \Bigg[V\left(\frac{2\sin\theta}{\lambda_1} - q_i, \sqrt{(1+0.0692x)(1-x)\Gamma_i^2 + (\Gamma_G^{\text{inst}})^2}, x\Gamma_i + \Gamma_L^{\text{inst}}\right) + 0.5V\left(\frac{2\sin\theta}{\lambda_2} - q_i, \sqrt{(1+0.0692x)(1-x)\Gamma_i^2 + (\Gamma_G^{\text{inst}})^2}, x\Gamma_i + \Gamma_L^{\text{inst}}\right)\Bigg] \tag{3.21}$$

Formula (3.21) already includes K_α doublet of the X-ray source (copper), with known wavelengths $\lambda_1 = 1.5406\,\text{Å}$, $\lambda_2 = 1.5444\,\text{Å}$. Amplitudes A_i and widths Γ_i for each diffraction can be either freely fitted or mutually constrained. The values of q_i are calculated from (3.6), and the lattice parameter a is fitted as well.

The particle size is then calculated from the width Γ_i, as described in section 3.1.2:

$$D = \frac{1.10}{\Gamma_i} \tag{3.22}$$

This expression can also be reformulated by means of the width in 2θ space ($\Gamma_{2\theta}$) to obtain the familiar Scherrer equation

$$\Gamma_i = \frac{\mathrm{d}q}{\mathrm{d}(2\theta)}\Gamma_{2\theta} = \frac{\cos\theta}{\lambda}\Gamma_{2\theta} \qquad \rightarrow \qquad D = \frac{1.10\lambda}{\Gamma_{2\theta}\cos\theta} \tag{3.23}$$

The constant 1.10 is clearly different from 0.94, usually proposed for spherical particles. Therefore, the detailed derivation presented in the preceding sections was intended, inter alia, to justify the utilized formula, which leads to better agreement with the size obtained by transmission electron microscopy (TEM).

3.2 Mössbauer spectroscopy

Mössbauer spectroscopy is based on resonant γ-ray absorption by atomic nuclei in a crystal lattice. Each nuclide (i.e. element with given proton and neutron numbers) has its characteristic energy-level scheme, and besides ground state, there is a large number of excited levels, spontaneously decaying into lower levels or even different nuclides, and having broadly varying half-lives. Since the structure of atomic nuclei is only very weakly influenced by external factors, the spectral width of the excited levels is very small. Therefore, the level scheme is usually deduced from the energy and angular correlations of *emitted* γ rays. There are, however, certain nuclides where measurement of resonant *absorption* is experimentally viable and convenient, such as ^{57}Fe and ^{119}Sn, which are therefore utilized in Mössbauer spectroscopy. The basic requirement comes from the possibility of recoil-less absorption, which requires that the momentum imparted by absorbed photon is not sufficient to excite lattice vibration (phonon).

The abundance of ^{57}Fe in natural iron is 2.2%. The excited state at 14.4 keV is produced as a β-decay product of ^{57}Co, which has half life $T_{1/2} = 271.7$ days, and emits the corresponding γ (14.4 keV) photon in 9.2% of decays (it also emits 122 keV and other photons, which are electronically excluded during the measurement). The ground state and the 14.4 keV excited state are depicted in Fig. 3.4, with their parity π, spin I, its projection m, mean life $\tau = T_{1/2}/\ln 2$, magnetic dipole (μ) and electric quadrupole (Q) moments [47]. Magnetic dipole

moments are given in their highest projection ($m = I$), in the units of nuclear magneton $\mu_N = 5.050784 \times 10^{-27}$ J/T. The transition in question is almost pure M1 (magnetic dipole, 1^+) transition, and the E2 (electric quadrupole, 2^+) contribution is negligible, therefore, it is not necessary to count, e.g., with a $-1/2 \to +3/2$ line.

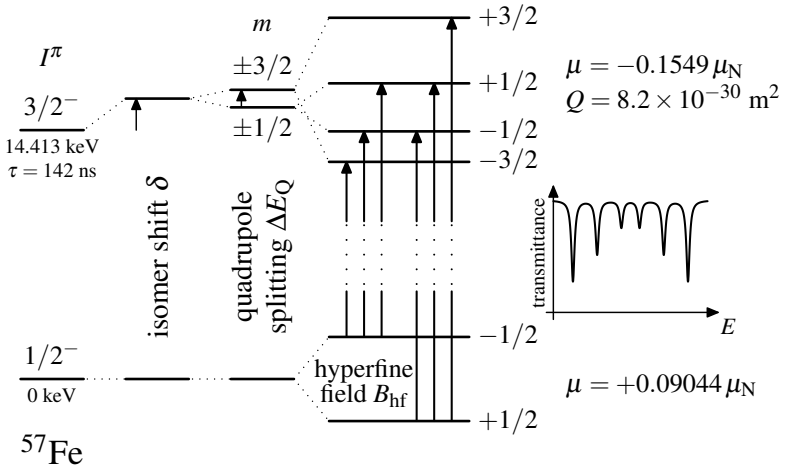

Figure 3.4: Level scheme and splitting of ^{57}Fe in external fields relevant to Mössbauer spectroscopy.

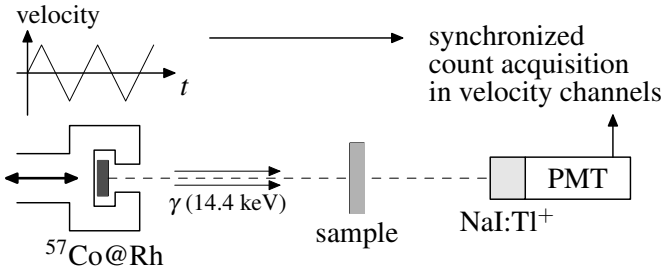

Figure 3.5: Mössbauer spectroscopy setup. The relevant γ rays (14.4 keV) are produced in the decay of ^{57}Co, embedded in rhodium, and their energy is fine-tuned by Doppler shift, driving the source by triangular velocity profile, with the amplitude of ca. 12 mm/s. Transmitted γ photons are detected in the NaI:Tl$^+$ scintillator with attached photomultiplier tube

The actual measurement setup is schematically depicted in Fig. 3.5. The acquired γ pulses are recorded (after energy discrimination) into a histogram, depending on the actual velocity of the source at the moment of detection. Energy is then usually given in the units of velocity (mm/s), due to almost linear dependence of E and v in the region of small Doppler shifts:

$$E = E_0 \sqrt{\frac{c+v}{c-v}} \approx E_0 \left(1 + \frac{v}{c}\right) \tag{3.24}$$

The histogram is then usually fitted with Lorentzian peaks, whose width is given mainly by the finite life-time of the excited state. This spectral width (Γ) can be

obtained by Fourier transforming the excited state wavefunction:

$$\int_0^\infty \psi(t)\mathrm{e}^{\mathrm{i}Et/\hbar}\mathrm{d}t \sim \int_0^\infty \mathrm{e}^{-t/2\tau+\mathrm{i}Et/\hbar}\mathrm{d}t = \frac{1}{1/2\tau - \mathrm{i}E/\hbar} \quad \xrightarrow{|\ |^2} \quad \frac{1}{(E/\hbar)^2 + (1/2\tau)^2}, \tag{3.25}$$

thus leading to Lorentzian energy distribution, having a width

$$\Gamma = \hbar/\tau = 7.43 \times 10^{-28}\ \mathrm{J} \Rightarrow 0.096\ \mathrm{mm/s\ at\ 14.4\ keV} \tag{3.26}$$

In fact, the observed width is at least two-fold, due to convolution of source and target spectral width.

The following parameters, which give useful structural information about iron [48], can be obtained by fitting the Mössbauer spectra (see also Fig. 3.4):

- isomer shift δ (mm/s), which reflects the monopolar part of electron density in the nuclear volume, due to slightly different radial proton distribution in the ground and excited state of ^{57}Fe. Reference value of $\delta = 0$ corresponds to metallic iron (Fe^0). In general, isomer shift gives a good information about valence state of iron: Fe^{2+} gives 0.8–1.2, Fe^{3+} gives 0.3–0.5, and Fe^{6+} gives negative values.

- quadrupole splitting ΔE_Q (mm/s) affects only the excited state (reasons are given below) and gives an information about quadrupolar part of electric field. It can reach values as large as 2, but it tends to be close to zero in magnetically ordered materials.

- hyperfine field B_hf (Tesla) is present in the nucleus due to broken symmetry of spin-up and spin-down electrons in magnetically ordered materials (ferro-, antiferro- and ferrimagnetic), and leads to a sextet in the measured spectra. B_hf reaches values around 50 T, which are in opposite direction to the net magnetic moment of the atom. This fact can be explained by spatial spreading of the electrons with aligned spins due to their exchange interactions with neighboring atoms, so the Coulomb force makes the electrons with opposite spin achieve higher density in the nucleus. The conversion of energy scale into magnetic field can be done by a formula $E = -\vec{\mu} \cdot \vec{B}$, using magnetic moments given in Fig. 3.4.

Presence of various symmetrically and chemically nonequivalent iron atoms or ions in crystal lattice can make the fitting of Mössbauer spectra a non-trivial task. Additional complications can arise due to relaxation of magnetic moments, however, even in such case the Mössbauer spectroscopy can provide useful insight into magnetization dynamics on the 10^{-7} s scale.

3.2.1 Angular momentum analysis of the Mössbauer spectrum

Further discussion of the Mössbauer levels, their splitting and intensity proportions, needs a more rigorous quantum-mechanical analysis. The discussion below works with the standard theory of angular momentum, which can be found in any decent textbook of quantum mechanics, e.g. [49, 50]. Notation of Clebsch-Gordan

coefficients is adopted from [51]. I will first analyze splitting by magnetic field, and then the quadrupole splitting.

The process of photon absorption (having angular momentum $J = 1$ and its projection M) in the ground state ($I_i = 1/2$, projection m_i) to get excited state ($I_f = 3/2$, projection m_f) can be described by angular momentum coupling:

$$|\tfrac{3}{2}, m_f\rangle = \sum_{m_i,M} C^{\frac{3}{2},m_f}_{\frac{1}{2},m_i,1,M} |\tfrac{1}{2}, m_i\rangle |1, M\rangle, \tag{3.27}$$

where the Clebsch-Gordan coefficient ($C^{\cdots}_{\cdots}$) is non-zero only when the angular momentum is conserved, i.e. $m_i + M = m_f$. The state $|\frac{3}{2}, m_f\rangle$ should not be confused with the excited state $^{57}\mathrm{Fe}^*$ (it is only a symmetrically adapted combination of the initial state and the photon), nevertheless, the Wigner-Eckart theorem guarantees that they have a constant overlap, not depending on m_f.

Clebsch-Gordan coefficients $C^{\cdots}_{\cdots}$ can be found in tables or conveniently derived employing the following relation for rising and lowering operators:

$$\hat{J}_\pm |jm\rangle = \sqrt{(j \mp m)(j \pm m + 1)}\, |j, m \pm 1\rangle \tag{3.28}$$

Formula (3.27) can be thus expanded as follows:

$$\begin{aligned}
|\tfrac{3}{2}, \tfrac{3}{2}\rangle &= |\tfrac{1}{2}, \tfrac{1}{2}\rangle |1, 1\rangle \\
|\tfrac{3}{2}, \tfrac{1}{2}\rangle &= \sqrt{\tfrac{1}{3}} \left(\sqrt{2}\, |\tfrac{1}{2}, \tfrac{1}{2}\rangle |1, 0\rangle + |\tfrac{1}{2}, -\tfrac{1}{2}\rangle |1, 1\rangle\right) \\
|\tfrac{3}{2}, -\tfrac{1}{2}\rangle &= \sqrt{\tfrac{1}{3}} \left(|\tfrac{1}{2}, \tfrac{1}{2}\rangle |1, -1\rangle + \sqrt{2}\, |\tfrac{1}{2}, -\tfrac{1}{2}\rangle |1, 0\rangle\right) \\
|\tfrac{3}{2}, -\tfrac{3}{2}\rangle &= |\tfrac{1}{2}, -\tfrac{1}{2}\rangle |1, -1\rangle
\end{aligned} \tag{3.29}$$

Obtained coefficients will be substituted into the Wigner-Eckart theorem

$$\langle \alpha', j', m' | \hat{T}_{\lambda\mu} | \alpha, j, m \rangle = \frac{1}{\sqrt{2j' + 1}} \langle \alpha', j' || \hat{T}_\lambda || \alpha, j \rangle C^{j',m'}_{j,m,\lambda,\mu} \tag{3.30}$$

applied to our system:

$$\langle {}^{57}\mathrm{Fe}^*, m_f | \hat{T}^{(\mathrm{M1})}_{1,M} | {}^{57}\mathrm{Fe}, m_i \rangle = \tfrac{1}{2} \langle {}^{57}\mathrm{Fe}^* || \hat{T}^{(\mathrm{M1})} || {}^{57}\mathrm{Fe} \rangle \; C^{\frac{3}{2},m_f}_{\frac{1}{2},m_i,1,M} \tag{3.31}$$

where $\langle {}^{57}\mathrm{Fe}^* || \hat{T}^{(\mathrm{M1})} || {}^{57}\mathrm{Fe} \rangle$ is the reduced matrix element of Mössbauer transition (independent on m_i, M, m_f, and can be calculated or measured for any such set) and $\hat{T}^{(\mathrm{M1})}$ is an operator corresponding to magnetic dipolar transition. Transition probability can be obtained by squaring the matrix element (3.31). If I assume the proportion of the photons with $M = -1$, 0, 1 to be $x_{-1} : x_0 : x_1$, then the rate of the first three transitions in Fig. 3.4 (excitations of the $m_i = -1/2$ level) is

$$\left(C^{\frac{3}{2},-\frac{3}{2}}_{\frac{1}{2},-\frac{1}{2},1,-1}\right)^2 x_{-1} : \left(C^{\frac{3}{2},-\frac{1}{2}}_{\frac{1}{2},-\frac{1}{2},1,0}\right)^2 x_0 : \left(C^{\frac{3}{2},\frac{1}{2}}_{\frac{1}{2},-\frac{1}{2},1,1}\right)^2 x_1 = 3x_{-1} : 2x_0 : 1x_1 \tag{3.32}$$

In the case of random orientation of the quantization axis (i.e. of the hyperfine field), the photons are in equal proportion, and the observed ratio is $3 : 2 : 1$. If the hyperfine field is fixed in the direction of optical axis (e.g. by a longitudinal arrangement of external magnetic field), then the photons in this direction can

have only two projections of their spin: $+1$ and -1 (right and left circular polarization). The observed ratio is then $3:0:1$. However, the measurements in the present thesis were done in perpendicular arrangement, so it is necessary to rotate the reference frame to the direction of the field.

Starting reference frame has its z-axis (quantization axis) in the direction of photon motion, so $M = \pm 1$. Rotation of the reference frame around y-axis through angle θ can be described by multiplication of photon state with a matrix

$$R_y(\theta) = \mathrm{e}^{\mathrm{i}\theta\hat{S}_y} = \exp\frac{\theta}{\sqrt{2}}\begin{pmatrix} 0 & 1 & 0 \\ -1 & 0 & 1 \\ 0 & -1 & 0 \end{pmatrix} \tag{3.33}$$

where the spin matrix $\hat{S}_y$ (expressed in the basis $|1,1\rangle$, $|1,0\rangle$, $|1,-1\rangle$) was derived from a relation $\hat{S}_\pm = \hat{S}_1 \pm \mathrm{i}\hat{S}_y$ using (3.28):

$$\hat{S}_\pm|1,0\rangle = \sqrt{2}\,|1,\pm1\rangle, \qquad \hat{S}_\pm|1,\mp1\rangle = \sqrt{2}\,|1,0\rangle, \tag{3.34a}$$

$$\hat{S}_+ = \begin{pmatrix} 0 & \sqrt{2} & 0 \\ 0 & 0 & \sqrt{2} \\ 0 & 0 & 0 \end{pmatrix}, \qquad \hat{S}_- = \begin{pmatrix} 0 & 0 & 0 \\ \sqrt{2} & 0 & 0 \\ 0 & \sqrt{2} & 0 \end{pmatrix} \tag{3.34b}$$

$$\hat{S}_y = \frac{\mathrm{i}(\hat{S}_- - \hat{S}_+)}{2} = \frac{\mathrm{i}}{\sqrt{2}}\begin{pmatrix} 0 & -1 & 0 \\ 1 & 0 & -1 \\ 0 & 1 & 0 \end{pmatrix} \tag{3.35}$$

Evaluation of matrix exponential in (3.33) requires its expansion into Taylor series. Fortunately, the terms in this series will repeat,

$$\hat{S}_y^2 = \frac{1}{2}\begin{pmatrix} 1 & 0 & -1 \\ 0 & 2 & 0 \\ -1 & 0 & 1 \end{pmatrix}, \quad \hat{S}_y^3 = \frac{\mathrm{i}}{\sqrt{2}}\begin{pmatrix} 0 & -1 & 0 \\ 1 & 0 & -1 \\ 0 & 1 & 0 \end{pmatrix} = \hat{S}_y, \quad \hat{S}_y^4 = \hat{S}_y^2, \ldots \tag{3.36}$$

so the result can be resummed into sines and cosines:

$$\begin{aligned} R_y(\theta) &= \frac{1}{2}\begin{pmatrix} 1 & 0 & -1 \\ 0 & 2 & 0 \\ -1 & 0 & 1 \end{pmatrix}\cos\theta + \frac{1}{2}\begin{pmatrix} 1 & 0 & 1 \\ 0 & 0 & 0 \\ 1 & 0 & 1 \end{pmatrix} + \mathrm{i}\hat{S}_y \sin\theta \\ &= \frac{1}{2}\begin{pmatrix} 1+\cos\theta & \sqrt{2}\,\sin\theta & 1-\cos\theta \\ -\sqrt{2}\,\sin\theta & 2\cos\theta & \sqrt{2}\,\sin\theta \\ 1-\cos\theta & -\sqrt{2}\,\sin\theta & 1+\cos\theta \end{pmatrix} \end{aligned} \tag{3.37}$$

If I assume non-polarized beam (equal proportion of $M = \pm 1$), then the ratio of the transition from $m_i = -1/2$ to $m_f = \mp 1/2$ (i.e. the second and the third peak) will be

$$\frac{\text{second}}{\text{third}} = 2\frac{x_0}{x_1} = 2\frac{2 \times \frac{1}{2}\sin^2\theta}{\frac{1}{4}[(1+\cos\theta)^2 + (1-\cos\theta)^2]} = \frac{4\sin^2\theta}{1+\cos^2\alpha} \tag{3.38}$$

which agrees with the result given e.g. in [19]. In particular, $\theta = \pi/2$ (perpendicular arrangement) gives the ratio $3:4:1$ for the first three lines.

Finally, the quadrupole splitting is caused by the non-zero quadrupole moment of the excited state, which is sensitive to the inhomogeneity of the electric field.

I will begin with a multipolar decomposition of electric potential $\varphi(\vec{r})$ in the volume of nucleus, using the spherical harmonics $Y_{lm}(\theta, \phi)$

$$\varphi(\vec{r}) = \sum_{\lambda=0}^{\infty} \sum_{\mu=-\lambda}^{+\lambda} \varphi_{\lambda\mu}(r) Y_{\lambda\mu}(\theta, \phi) \tag{3.39}$$

Dipolar component ($\lambda = 1$) is zero in the equilibrium position of the nucleus, while quadrupolar component ($\lambda = 2$) will be taken in the long-wave limit for simplicity ($\varphi_{2\mu}$ are some constants):

$$\varphi_{2\mu}(r) \approx \varphi_{2\mu} r^2, \qquad r^2 Y_{2,0}(\theta, \phi) = \sqrt{5/16\pi}\,(2z^2 - x^2 - y^2), \text{ etc.} \tag{3.40}$$

The ground state is unaffected by $\varphi_{2\mu}$, because

$$\langle \tfrac{1}{2}, m' | r^2 Y_{2\mu} | \tfrac{1}{2}, m \rangle = 0 \tag{3.41}$$

due to Wigner-Eckart theorem (3.30) (the triangular inequality is not satisfied). If the excited state is already split by the magnetic field, and the quadrupole interaction can be considered small, then (by first-order perturbation theory) the energy is affected only by the φ_{20} component (i.e. the electric field gradient in the direction of magnetic field)

$$\Delta E \propto \langle \tfrac{3}{2}, m | r^2 Y_{2,0} | \tfrac{3}{2}, m \rangle \propto C^{\frac{3}{2},m}_{\frac{3}{2},m,2,0} = \begin{cases} \sqrt{1/5} & \text{for } m = \pm 3/2 \\ -\sqrt{1/5} & \text{for } m = \pm 1/2 \end{cases} \tag{3.42}$$

If there is no magnetic field, then the excited state is split into two levels. In the case of axially symmetric quadrupole field, the symmetry axis is chosen as the z-direction and the splitting into degenerated doublet of $m = \pm 1/2$ and $\pm 3/2$ is obtained according to (3.42) and Fig. 3.4. If the quadrupole field is not axially symmetric, then the perturbation theory for degenerated spectra has to be used, nevertheless, the result is again a degenerate doublet, but not longer with definite values of m.

4. Discussion and results

This chapter provides detailed discussion of the chemistry of the hydrothermal synthesis and subsequent modifications. Physical properties are sufficiently discussed in the articles [A1–3], with detailed introduction given in the previous chapters.

4.1 Precursors and conditions of the hydrothermal method

The synthesis of cobalt and iron oxide, which was investigated in the present work, involves hydrothermal treatment of metal salts and sodium oleate / oleic acid in a solvent composed of water and alcohol. The reactions which take place even before heating are

$$\begin{aligned} \mathrm{Fe(NO_3)_3} + 3\,\mathrm{Na(oleate)} &\rightarrow \mathrm{Fe(oleate)_3} + 3\,\mathrm{NaNO_3} \\ \mathrm{FeCl_2} + 2\,\mathrm{Na(oleate)} &\rightarrow \mathrm{Fe(oleate)_2} + 2\,\mathrm{NaCl} \\ \mathrm{Co(NO_3)_2} + 2\,\mathrm{Na(oleate)} &\rightarrow \mathrm{Co(oleate)_2} + 2\,\mathrm{NaNO_3} \end{aligned} \tag{4.1}$$

Liquid precursors are poured into a 45 ml teflon vessel and enclosed in a stainless steel autoclave (Berghof DAB-3), which is able to sustain temperatures up to 250°C. The essential components, which take place in the reaction, are depicted in Fig. 4.1.

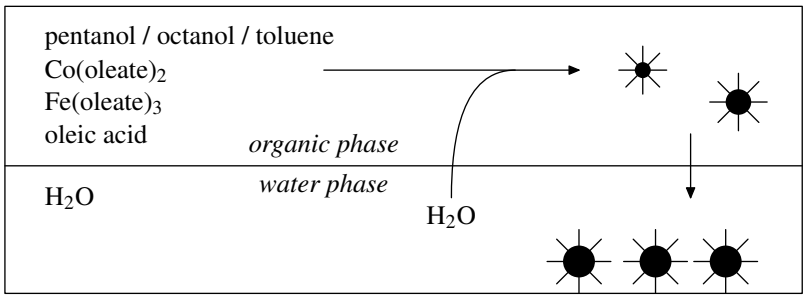

Figure 4.1: Mechanism of the hydrothermal synthesis of cobalt ferrite: metal oleates are hydrolyzed, and the growing particles precipitate into water phase after reaching critical diameter, which can be controlled by polarity of organic phase.

In the course of investigation of the mechanism, the following approaches were applied, and are given here in the order of increasing quality of the product:

1. a solution of sodium oleate and oleic acid in water + alcohol was mixed with a water solution of metal nitrates, and then treated hydrothermally [A1]

2. after mixing sodium oleate and metal nitrate solutions, the resultant slurry was briefly sonicated, water phase was removed, and certain amount of pure water added, optionally containing sodium oleate and sodium chloride [A2]

3. pentanol solution of metal oleates was prepared beforehand by refluxing metal salts with sodium oleate; this solution is then treated hydrothermally, together with some water [A3]

Detailed procedures for these approaches are given in the attached publications. Best results can be obtained by the third approach, which leads to the best monodispersity and phase purity (see Fig. 4.2), and almost no irreversible precipitation during cleaning of the product, as compared to the previous two approaches. Here, I will discuss some aspects which influence the outcome, and are essential for a successful design of the synthesis. These investigations were done employing the first two approaches to precursor preparation.

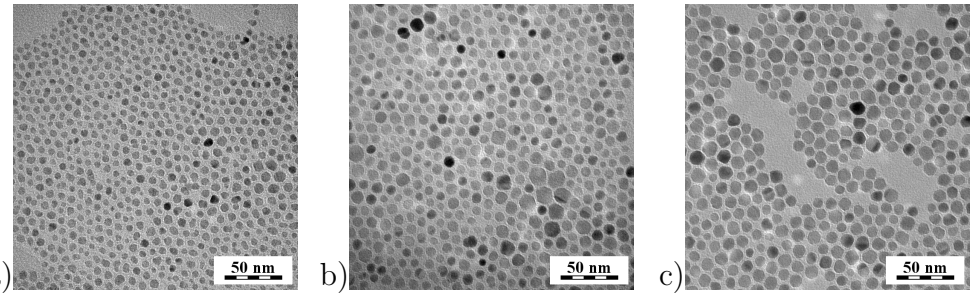

Figure 4.2: Cobalt ferrite particles prepared by the hydrothermal hydrolysis of cobalt-iron oleate in pentanol/octanol/toluene + water at 180 or 220 °C. Volume-weighted average diameters are 6.2, 9.1 and 10.5 nm, respectively, and increase with decreasing polarity of the solvent and higher temperature. As-prepared particles are coated with oleic acid, which provides uniform inter-particle spacing of ca. 2.5 nm.

First, it has to be noted that after synthesis the prepared particles are found sedimented on the bottom of the vessel, they are surface-coated with oleic acid and are hydrophobic. They can be dispersed in organic solvents, like hexane, cyclohexane and toluene. However, addition of ethanol or acetone induces their precipitation. It was found that higher proportion of ethanol is needed in the case of smaller particles. It was therefore deduced that the polarity of organic phase plays an important role also during the synthesis, controlling the final size of the particles, as described in Fig. 4.1 and [A1]. Pentanol was chosen as a suitable solvent, providing enough polarity for the precipitation of the product during the synthesis, dissolving the initial metal oleates, and weakly miscible with water.

Due to a requirement of high batch yield and narrow distribution of particle size, it is also necessary to ensure constant conditions during the course of the synthesis by choosing an appropriate concentration of the precursors in the organic phase. I usually used 3 mmol of metal ions per 10 ml of organic solvent (pentanol/octanol/toluene), which provided satisfactory results, whereas 6 mmol of M^{n+} per 10 ml of pentanol led to a somewhat less regular product (Fig. 4.3a). In this respect, ethanol is not a suitable solvent, because it remains mostly in the water phase, and the hydrolysis of metal oleates occurs in their concentrated form, leading to a substantial amount of very polydisperse particles remaining in the organic phase (Fig. 4.3b). I tried also to increase the polarity of organic phase by using a mixture of pentanol and ethanol, however, the average size of the particles was the same as with pure pentanol (by XRD), with broader distribution (Fig. 4.3c)

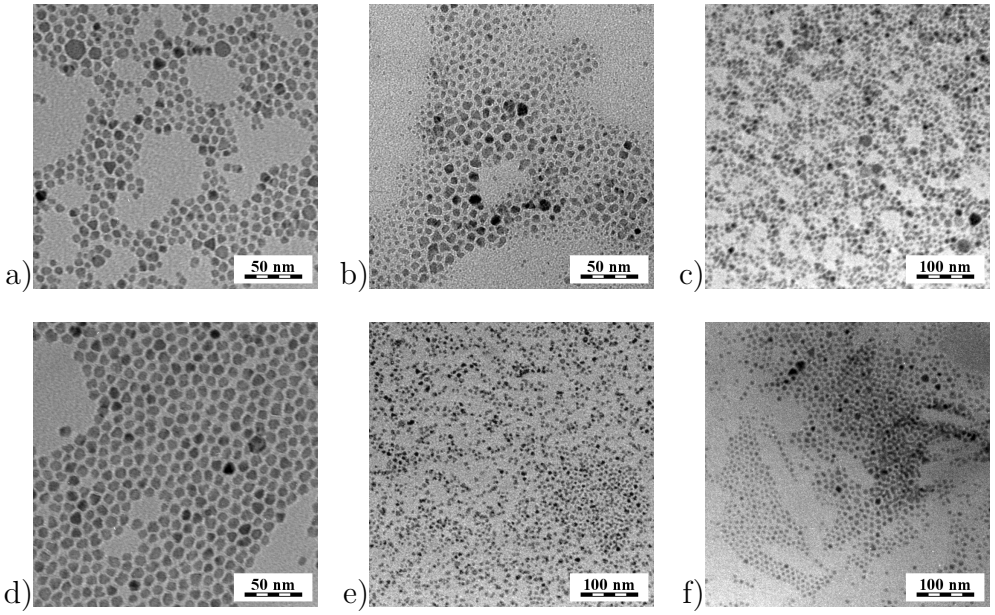

Figure 4.3: TEM pictures of $CoFe_2O_4$ nanoparticles to illustrate the influence of reaction conditions (all at 200°C except b)): a) synthesis with 6 mmol of metal ions per 10 ml of pentanol, b) particles which remain in organic phase after using ethanol (180°C), c) synthesis in 15 ml pentanol + 10 ml ethanol + 2 ml water, d) synthesis using two-step seed growth in 20 ml toluene + 6 ml ethanol + 0.5 ml water, e) synthesis in 25 ml pentanol and no water, f) directly hydrophilic particles obtained in 15 ml pentanol + 10 ml water with 2 mmol of sodium oleate.

Polarity of the organic phase can be decreased by adding octanol or toluene. In that case, certain amount of not-fully-grown particles remains in the organic phase after hydrothermal treatment, and should be discarded not to deteriorate the size distribution of the product. If the reaction is done at 180°C, the particles don't even grow enough to precipitate, and have a diameter of 6 nm in all cases. To prepare larger particles (up to 10 nm), it is necessary to use either seed-mediated growth (dispersing certain amount of pre-synthesized particles in octanol or toluene, and adding them to the reaction) [A2], see Fig. 4.3d, or to use higher temperature, at least 220°C, which apparently provides higher rate of growth over nucleation [A3].

The water phase is also an important component of the synthesis (even as little as 0.5 ml). When no water is explicitly added, the particles grown in pentanol are very small (Fig. 4.3e). Water was therefore always added, also to physically separate the sedimented particles from the organic phase, usually in an amount of 5 or 10 ml (depending on the free space which was necessary due to thermal expansion of the liquids). When the water phase contained some sodium oleate (2 mmol per 10 ml) and no other inorganic salt, then the resulting particles were prepared in an unexpected form: they were completely dispersed in the water phase after hydrothermal treatment (TEM picture of such particles are shown in Fig. 4.3f) [A2]. Although such water dispersion appeared to be of high quality (not turbid and stable against sedimentation), it was not much suitable for further use, due to difficulties with the separation of excess sodium oleate (dialysis apparently didn't work for sodium oleate), and with instability towards precipi-

tation by salts (e.g. by 0.4 mM sodium chloride) or by ethanol. Nevertheless, hydrophilic magnetite prepared in this way was conveniently utilized for further ligand exchange with carboxymethyl dextran [A2].

4.2 Surface modifications

Since the prepared particles are hydrophobic, the main aim of the ligand exchange is to make them hydrophilic. One of the most common types of modification is the coating with silica (SiO_2) layer, which needs to be done in microemulsion-like environment [40], as opposed to Stöber process in polar solvents. Since silica coating was widely investigated by others, the present work focuses on suface modification by other compounds, namely: di- or tricarboxylic acids, carboxymethyl dextran and TiO_2. All products were subjected to dialysis (two times with 1 liter of water for 24 h) before further measurements (TEM, DLS, magnetic measurements).

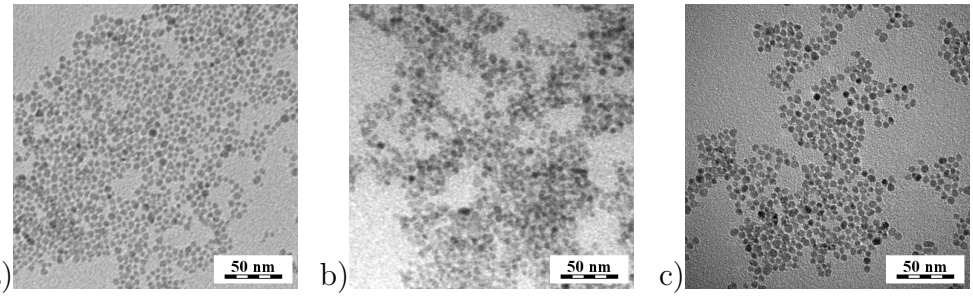

Figure 4.4: Cobalt ferrite particles (6 nm) surface-modified with a) 2,3-dimercaptosuccinig acid, b) L-tartaric acid, c) citric acid.

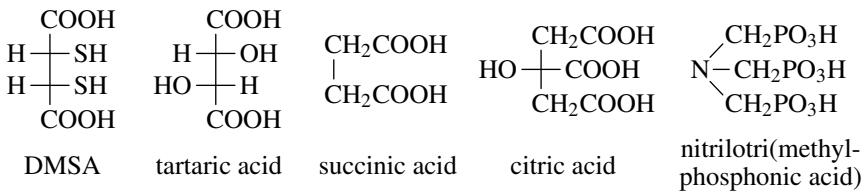

Figure 4.5: Carboxylic acids used for surface modification, and phosphonic acid for stabilization of TiO_2.

A ligand exchange with small carboxylic acid can be achieved in a mixed solvent of toluene (50 ml) and dimethylsulfoxide (5 ml). Di- or tricarboxylic acids were used (see Fig. 4.4, 4.5), since they are supposed to replace oleic acid due to chelate effect. Usually, 100 mg of the particles were dispersed in toluene, and the acid (100 mg) was dissolved in DMSO. Both liquids were mixed together (toluene and DMSO are miscible), sonicated for 5 min, and mechanically stirred at least for 24 hours. During that time, the particles sedimented, and were washed with ethanol and acetone with subsequent centrifugation. Addition of water (10 ml) leads to a cloudy dispersion, which can be cleared by increasing the pH. The best result is achieved for 2,3-dimercaptosuccinic acid (DMSA), increasing the pH with 0.2 mmol (8 mg) of NaOH, which leads to a very stable dispersion, which doesn't appear turbid even under strong illumination, and can be diluted with ethanol (to make it more suitable for TEM measurement; see Fig. 4.4a).

The hydrodynamic diameter (as measured by dynamic light scattering) is as low as 20 nm, down to pH 3 [A1]. Modification with succinic acid led to particles dispersible only in ethanol and not in water. Tartaric acid led to a cloudy dispersion (Fig. 4.4b), using only 0.05 mmol (2 mg) of NaOH (larger amount led to precipitation in a few seconds). Modification with citric acid and subsequent addition of 0.1 mmol (10 mg) of Na_2CO_3 led to a water dispersion stable for one week [A3]. Dilution with ethanol caused flocculation, whereas dilution with methanol increased stability to more than a month (Fig. 4.4c). Nevertheless, the water and methanol dispersions of citrate-coated particles appear partially turbid under strong illumination. The exceptional stability and clarity of dispersions of DMSA-coated particles, as compared to OH-terminated acids, can be probably explained by a formation of S–S bonds, which prevent detachment of the ligand under increased pH.

Carboxymethyl dextran (CM-dextran) was chosen for the modification of magnetite, since it provides suitable coating for use in biomedical applications. Since the toluene + DMSO solvent could not be used in this case, I utilized directly hydrophilic oleate-coated particles, as described in the previous section and [A2]. CM-dextran was prepared just before the modification by reacting dextran, NaOH and chloroacetic acid in water solution at 70 °C (Fig. 4.6). This solution was then added directly to hydrophilic magnetite and stirred for 26 h. Subsequent centrifugation led to a separation of soap-like upper layer (probably consisting of sodium oleate, oleic acid and pentanol), which was discarded. Water phase with partially sedimented particles was then subjected to dialysis, during which the sediment entered into a stable dispersion. The degree of substitution of CM-dextran (found as 0.5) was investigated by titration with 0.04 M NaOH (previously standardized with oxalic acid). Solid CM-dextran was obtained by acidifying the separately prepared CM-dextran solution with hydrochloric acid, and precipitating it with methanol. It is interesting that the pure CM-dextran (sodium salt), prepared in a similar way, was not efficient for ligand exchange. I suppose that the glycolic acid ($HOCH_2COOH$), created as a by-product, facilitated removal of oleic acid from the surface of precursor particles.

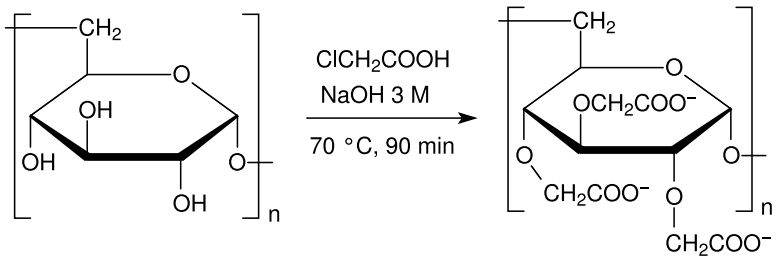

Figure 4.6: Preparation of carboxymethyl dextran. Practically achieved degree of substitution was around 0.5, instead of 3.

Finally, coating with TiO_2 was achieved by using titanium isopropoxide. Since titanium alkoxides hydrolyze immediately by traces of water, I didn't add water to the reaction directly. Titanium isopropoxide (0.5 ml) was added to a mechanically stirred toluene dispersion of $CoFe_2O_4$ particles (50 mg in 20 ml). Slow hydrolysis was then assumed by air humidity (60% at 20 °C), and led to precipitation after more than an hour ($CoFe_2O_4$ particles precipitated together with

TiO_2). Therefore, to avoid precipitation of a non-dispersible composite, a solution of nitrilotri(methylphosphonic acid) (1 mmol; 299 mg) in 5 ml of DMSO was added after 30 min of stirring (i.e. before precipitation), to protect the TiO_2 layer against agglomeration. After 24 h of stirring, the product was separated by centrifugation, washed with acetone and ethanol, and finally dispersed in water with 2 mmol (80 mg) of NaOH. Although the prepared slightly-turbid dispersion appears quite stable, the TEM images reveal network-like structure instead of core-shell morphology [A3]. And indeed, the preparation of sub-100 nm core-shell particles with titania proved to be difficult also by other authors [52, 53].

4.3 TEM and XRD analysis

The size of the particles in [A3] was evaluated according to the section 3.1. Previous articles [A1, A2] involved less sophisticated methods, so I present their re-evaluation in Fig. 4.7. The obtained diameters are slightly larger than in the previous evaluation, and better correspond to each other. The number given in parentheses for the TEM data represents the polydispersity, e.g. 6.3±1.3 nm, and was obtained by multiplication of the mean value with σ.

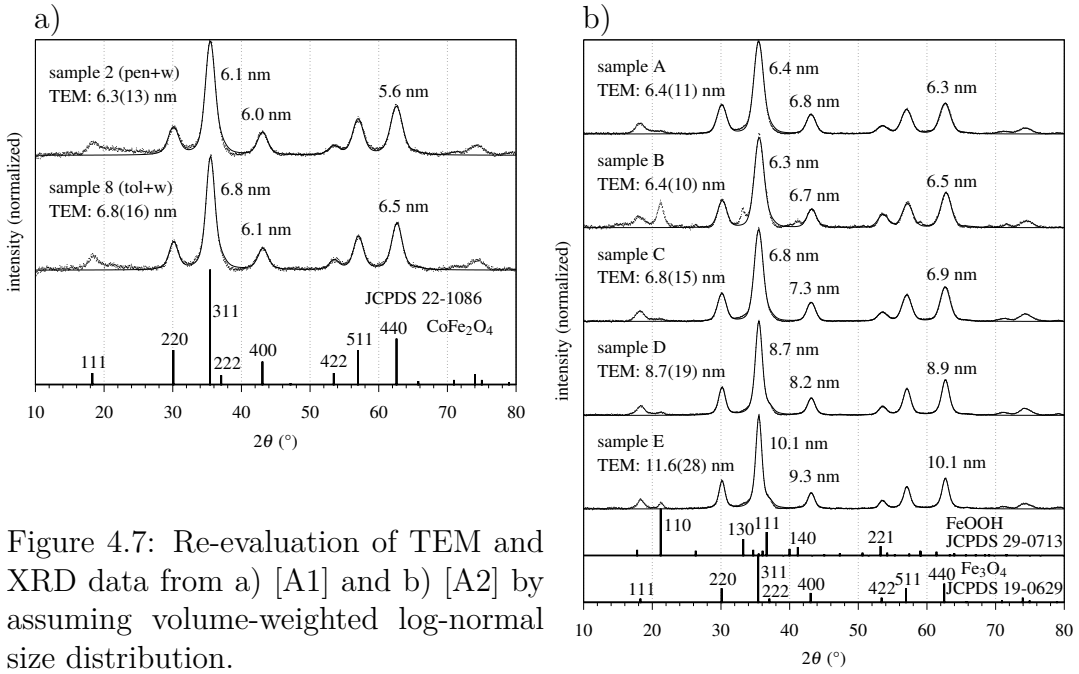

Figure 4.7: Re-evaluation of TEM and XRD data from a) [A1] and b) [A2] by assuming volume-weighted log-normal size distribution.

5. Conclusions

The hydrothermal method was developed in the present work to a point where it can be applied to a routine synthesis of high-quality nanoparticles of cobalt ferrite (and also magnetite) in 500 mg batches, in the size range of 6–10 nm. The synthesis and subsequent manipulation is much simpler than for the thermal decomposition widely utilized to date, although probably doesn't quite reach its monodispersity.

As a next step, various surface modifications were demonstrated, namely with dimercaptosuccinic acid, citric acid, carboxymethyl dextran and TiO_2, and provide a good overview of the possibilities of ligand exchange for this type of nanoparticles.

The need for reproducible analysis of X-ray diffractograms, to obtain the average particle size, led to the development of a `gnuplot` script (given in Attachments), which can be easily adapted for routine analysis of batches of similar samples.

Finally, the prepared nanoparticles provided a good material for investigation of superparamagnetism and inter-particle interactions. These interactions were shown to significantly influence the magnetic properties and should be taken into account when analyzing the magnetization data of such materials.

List of Abbreviations

AC – alternating current
CM-dextran – carboxymethyl dextran
DLS – dynamic light scattering
DMSA – 2,3-dimercaptosuccinic acid
DMSO – dimethylsulfoxide
FC – field cooled (magnetization)
SQUID – superconducting quantum interference device (a type of magnetometer)
TEM – transmission electron microscopy
XRD – (powder) X-ray diffraction
ZFC – zero field cooled (magnetization)

Attachments

The following articles present the results of the current thesis, and are attached after the bibliography. A.R. (as a corresponding author of all three articles) carried out all the syntheses, wrote 90% of the manuscripts, and evaluated the measured data. The characterizations (except XRD and DLS) and their initial evaluation was provided by the co-authors.

[A1] A. Repko, D. Nižňanský, J. Poltierová-Vejpravová: A study of oleic acid-based hydrothermal preparation of $CoFe_2O_4$ nanoparticles. *Journal of Nanoparticle Research* **13** (2011), 5021–5031. doi:10.1007/s11051-011-0483-z

[A2] A. Repko, D. Nižňanský, I. Matulková, M. Kalbáč, J. Vejpravová: Hydrothermal preparation of hydrophobic and hydrophilic nanoparticles of iron oxide and a modification with CM-dextran. *Journal of Nanoparticle Research* **15** (2013), 1767 (9 pp). doi:10.1007/s11051-013-1767-2

[A3] A. Repko, J. Vejpravová, T. Vacková, D. Zákutná, D. Nižňanský: Superparamagnetic properties of hydrothermally prepared $CoFe_2O_4$ as a function of size (6-10 nm) and coating (oleic/citric acid or TiO_2). Submitted to *Journal of Magnetism and Magnetic Materials* (2014).

Example script for XRD fitting in `gnuplot`

```
set terminal png
set angles degrees; set samples 500
set xlabel '2 theta'; set ylabel 'intensity (normalized)'
set xtics out; set mxtics; set grid lt 18

infile='AR14_40A-5000s-30.ASC'
ampl=91.6
set output 'AR14_40A.png'

lambda1=1.5406; lambda2=1.5444; k2=0.5
res_g=0.0065; res_l=0.003        # instrumental width
m(x)=1.000599-0.1164/(x+14.73)   # peak position correction
qn(n,a)=10*sqrt(n)/a             # n=h^2+k^2+l^2
qth1(x)=20*sin(x/2)/lambda1      # x=2theta
qth2(x)=20*sin(x/2)/lambda2
th1(n,a)=2*asin(lambda1*sqrt(n)/(2*a))
th2(n,a)=2*asin(lambda2*sqrt(n)/(2*a))
sql2=sqrt(log(2))
voi(x,dg,dl)=voigt(sql2*2*x/dg,sql2*dl/dg)*(dg+dl)/dg
# w(dg,dl)=0.5346*dl+sqrt(0.2166*dl*dl+dg*dg)
dg(w,L)=sqrt(w*w*(1-L)*(1+0.0692*L)+res_g*res_g)
peak(x,a,n,w,L)=voi(qth1(x)-qn(n,a),dg(w,L),w*L+res_l)\
  +k2*voi(qth2(x)-qn(n,a),dg(w,L),w*L+res_l)
d(w) = 1.1/w
```

```
# constrain: 311-511-422-222(1)  440-220-531(2)  400(3)
f1(x) = c1*peak(x,a,8,w2,L)  # 220
f2(x) = c2*(peak(x,a,11,w1,L)+0.05*peak(x,a,12,w1,L))  # 311 222
f3(x) = c3*peak(x,a,16,w3,L)  # 400
f4(x) = c4*peak(x,a,24,w1,L)  # 422
f5(x) = c5*peak(x,a,27,w1,L)  # 511
f6(x) = c6*(peak(x,a,32,w2,L)+0.025*peak(x,a,35,w2,L))  # 440 531

c1=16; c2=66; c3=12; c4=4; c5=16; c6=22
w1=0.2; w2=0.2; w3=0.2; L=0.4; p=-0.5
a=8.4
fit [28:66] f1(x)+f2(x)+f3(x)+f4(x)+f5(x)+f6(x)+p infile\
  u ($1*m($1)):($2/ampl) via c1,c2,c3,c4,c5,c6,w1,w2,w3,a,L,p

set label '%.1f nm', d(w1) at 37,70
set label '%.1f nm', d(w2) at 60,40
set label '%.1f nm', d(w3) at 40,25
set label 'lorentz: %.2f', L at 51,72
set label 'a = %.3f A', a at 51,65

plot [10:80][0:100] infile u ($1*m($1)):($2/ampl) w d t infile,\
  f1(x)+f2(x)+f3(x)+f4(x)+f5(x)+f6(x)+p w l lt -1 notitle
```

Bibliography

[1] L. H. Reddy, J. L. Arias, J. Nicolas, and P. Couvreur: Magnetic Nanoparticles: Design and Characterization, Toxicity and Biocompatibility, Pharmaceutical and Biomedical Applications. *Chemical Reviews* **112** (2012) 5818–5878. doi:10.1021/cr300068p.

[2] M. Knobel, W. C. Nunes, L. M. Socolovsky, E. De Biasi, J. M. Vargas, and J. C. Denardin: Superparamagnetism and other magnetic features in granular materials: A review on ideal and real systems. *Journal of Nanoscience and Nanotechnology* **8** (2008) 2836–2857. doi:10.1166/jnn.2008.017.

[3] S. Bedanta and W. Kleemann: Supermagnetism. *Journal of Physics D: Applied Physics* **42** (2009) 013001. doi:10.1088/0022-3727/42/1/013001.

[4] H. Shenker: Magnetic Anisotropy of Cobalt Ferrite ($Co_{1.01}Fe_{2.00}O_{3.62}$) and Nickel Cobalt Ferrite ($Ni_{0.72}Fe_{0.20}Co_{0.08}Fe_2O_4$). *Physical Review* **107** (1957) 1246–1249. doi:10.1103/PhysRev.107.1246.

[5] L. Bessais, L. Ben Jaffel, and J. L. Dormann: Relaxation time of fine magnetic particles in uniaxial symmetry. *Physical Review B* **45** (1992) 7805–7815. doi:10.1103/PhysRevB.45.7805.

[6] J. J. Lu, H. Y. Deng, and H. L. Huang: Thermal relaxation of interacting fine magnetic particles – field-cooled and zero-field-cooled magnetization variation. *Journal of Magnetism and Magnetic Materials* **209** (2000) 37–41. doi:10.1016/S0304-8853(99)00640-X.

[7] J. L. Tholence: On the frequency-dependence of the transition-temperature in spin-glasses. *Solid State Communications* **35** (1980) 113–117. doi:10.1016/0038-1098(80)90225-2.

[8] S. Shtrikman and E. P. Wohlfarth: The theory of the Vogel-Fulcher law of spin-glasses. *Physics Letters A* **85** (1981) 467–470. doi:10.1016/0375-9601(81)90441-2.

[9] J. Souletie and J. L. Tholence: Critical slowing down in spin-glasses and other glasses: Fulcher versus power law. *Physical Review B* **32** (1985) 516–519. doi:10.1103/PhysRevB.32.516.

[10] P. Allia, M. Coisson, P. Tiberto, F. Vinai, M. Knobel, M. A. Novak, and W. C. Nunes: Granular Cu-Co alloys as interacting superparamagnets. *Physical Review B* **64** (2001) 144420. doi:10.1103/PhysRevB.64.144420.

[11] O. Petracic, A. Glatz, and W. Kleemann: Models for the magnetic ac susceptibility of granular superferromagnetic $CoFe/Al_2O_3$. *Physical Review B* **70** (2004) 214432. doi:10.1103/PhysRevB.70.214432.

[12] N. Ballarini, F. Cavani, S. Passeri, L. Pesaresi, A. F. Lee, and K. Wilson: Phenol methylation over nanoparticulate $CoFe_2O_4$ inverse spinel catalysts: The effect of morphology on catalytic performance. *Applied Catalysis A: General* **366** (2009) 184–192. doi:10.1016/j.apcata.2009.07.003.

[13] X. Feng, G. Y. Mao, F. X. Bu, X. L. Cheng, D. M. Jiang, and J. S. Jiang: Controlled synthesis of monodisperse $CoFe_2O_4$ nanoparticles by the phase transfer method and their catalytic activity on methylene blue discoloration with H_2O_2. *Journal of Magnetism and Magnetic Materials* **343** (2013) 126–132. doi:10.1016/j.jmmm.2013.05.001.

[14] J. S. Chen, C. Chen, J. Liu, R. Xu, S. Z. Qiao, and X. W. Lou: Ellipsoidal hollow nanostructures assembled from anatase TiO_2 nanosheets as a magnetically separable photocatalyst. *Chemical Communications* **47** (2011) 2631–2633. doi:10.1039/c0cc04471g.

[15] V. Tyrpekl, J. P. Vejpravova, A. G. Roca, N. Murafa, L. Szatmary, and D. Niznansky: Magnetically separable photocatalytic composite gamma-Fe_2O_3@TiO_2 synthesized by heterogeneous precipitation. *Applied Surface Science* **257** (2011) 4844–4848. doi:10.1016/j.apsusc.2010.12.110.

[16] Q. Dai, D. Berman, K. Virwani, J. Frommer, P.-O. Jubert, M. Lam, T. Topuria, W. Imaino, and A. Nelson: Self-Assembled Ferrimagnet Polymer-Composites for Magnetic Recording Media. *Nano Letters* **10** (2010) 3216–3221. doi:10.1021/nl1022749.

[17] G. Liu, R. Y. Hong, L. Guo, Y. G. Li, and H. Z. Li: Preparation, characterization and MRI application of carboxymethyl dextran coated magnetic nanoparticles. *Applied Surface Science* **257** (2011) 6711–6717. doi:10.1016/j.apsusc.2011.02.110.

[18] N. Moumen, P. Veillet, and M. P. Pileni: Controlled preparation of nanosize cobalt ferrite magnetic particles. *Journal of Magnetism and Magnetic Materials* **149** (1995) 67–71. doi:10.1016/0304-8853(95)00340-1.

[19] A. T. Ngo, P. Bonville, and M. P. Pileni: Nanoparticles of $Co_xFe_y\square_zO_4$: Synthesis and superparamagnetic properties. *European Physical Journal B* **9** (1999) 583–592. doi:10.1007/s100510050801.

[20] V. Pillai, P. Kumar, M. J. Hou, P. Ayyub, and D. O. Shah: Preparation of nanoparticles of silver-halides, superconductors and magnetic-materials using water-in-oil microemulsions as nano-reactors. *Advances in Colloid and Interface Science* **55** (1995) 241–269. doi:10.1016/0001-8686(94)00227-4.

[21] A. J. Rondinone, A. C. S. Samia, and Z. J. Zhang: Superparamagnetic relaxation and magnetic anisotropy energy distribution in $CoFe_2O_4$ spinel ferrite nanocrystallites. *Journal of Physical Chemistry B* **103** (1999) 6876–6880. doi:10.1021/jp9912307.

[22] C. Liu, B. S. Zou, A. J. Rondinone, and J. Zhang: Chemical control of superparamagnetic properties of magnesium and cobalt spinel ferrite nanoparticles through atomic level magnetic couplings. *Journal of the American Chemical Society* **122** (2000) 6263–6267. doi:10.1021/ja000784g.

[23] Y. Lee, J. Lee, C. J. Bae, J. G. Park, H. J. Noh, J. H. Park, and T. Hyeon: Large-scale synthesis of uniform and crystalline magnetite nanoparticles using reverse micelles as nanoreactors under reflux conditions. *Advanced Functional Materials* **15** (2005) 503–509. doi:10.1002/adfm.200400187.

[24] S. Ammar, A. Helfen, N. Jouini, F. Fievet, I. Rosenman, F. Villain, P. Molinie, and M. Danot: Magnetic properties of ultrafine cobalt ferrite particles synthesized by hydrolysis in a polyol medium. *Journal of Materials Chemistry* **11** (2001) 186–192. doi:10.1039/b003193n.

[25] S. H. Sun, H. Zeng, D. B. Robinson, S. Raoux, P. M. Rice, S. X. Wang, and G. X. Li: Monodisperse MFe_2O_4 (M = Fe, Co, Mn) nanoparticles. *Journal of the American Chemical Society* **126** (2004) 273–279. doi:10.1021/ja0380852.

[26] J. Park, K. J. An, Y. S. Hwang, J. G. Park, H. J. Noh, J. Y. Kim, J. H. Park, N. M. Hwang, and T. Hyeon: Ultra-large-scale syntheses of monodisperse nanocrystals. *Nature Materials* **3** (2004) 891–895. doi:10.1038/nmat1251.

[27] N. Bao, L. Shen, W. An, P. Padhan, C. H. Turner, and A. Gupta: Formation Mechanism and Shape Control of Monodisperse Magnetic $CoFe_2O_4$ Nanocrystals. *Chemistry of Materials* **21** (2009) 3458–3468. doi:10.1021/cm901033m.

[28] D. Maity, S.-G. Choo, J. Yi, J. Ding, and J. M. Xue: Synthesis of magnetite nanoparticles via a solvent-free thermal decomposition route. *Journal of Magnetism and Magnetic Materials* **321** (2009) 1256–1259. doi:10.1016/j.jmmm.2008.11.013.

[29] A. P. Herrera, L. Polo-Corrales, E. Chavez, J. Cabarcas-Bolivar, O. N. C. Uwakweh, and C. Rinaldi: Influence of aging time of oleate precursor on the magnetic relaxation of cobalt ferrite nanoparticles synthesized by the thermal decomposition method. *Journal of Magnetism and Magnetic Materials* **328** (2013) 41–52. doi:10.1016/j.jmmm.2012.09.069.

[30] A. Mizuno, M. Takehara, J. Cuya, H. Miyamura, and B. Jeyadevan. Modified solvent-free thermal decomposition technique to synthesize monodispersed magnetite nanoparticles in wide size range. In *8th International Conference on Fine Particle Magnetism* (Perpignan, 24–27 June 2013), page 59, http://www.promes.cnrs.fr/ICFPM2013/Files/ICFPM_Booklet.pdf.

[31] X. Wang, J. Zhuang, Q. Peng, and Y.-D. Li: A general strategy for nanocrystal synthesis. *Nature* **437** (2005) 121–124. doi:10.1038/nature03968.

[32] X. Liang, X. Wang, J. Zhuang, Y. Chen, D. Wang, and Y. Li: Synthesis of nearly monodisperse iron oxide and oxyhydroxide nanocrystals. *Advanced Functional Materials* **16** (2006) 1805–1813. doi:10.1002/adfm.200500884.

[33] X.-H. Li, C.-L. Xu, X.-H. Han, L. Qiao, T. Wang, and F.-S. Li: Synthesis and Magnetic Properties of Nearly Monodisperse $CoFe_2O_4$ Nanoparticles Through a Simple Hydrothermal Condition. *Nanoscale Research Letters* **5** (2010) 1039–1044. doi:10.1007/s11671-010-9599-9.

[34] J. P. Ge, S. Xu, J. Zhuang, X. Wang, Q. Peng, and Y. D. Li: Synthesis of CdSe, ZnSe, and $Zn_xCd_{1-x}Se$ nanocrystals and their silica sheathed core/shell structures. *Inorganic Chemistry* **45** (2006) 4922–4927. doi:10.1021/ic051598k.

[35] H. Hu, Z. Chen, T. Cao, Q. Zhang, M. Yu, F. Li, T. Yi, and C. Huang: Hydrothermal synthesis of hexagonal lanthanide-doped LaF_3 nanoplates with bright upconversion luminescence. *Nanotechnology* **19** (2008) 375702. doi:10.1088/0957-4484/19/37/375702.

[36] F. Wang, Y. Han, C. S. Lim, Y. Lu, J. Wang, J. Xu, H. Chen, C. Zhang, M. Hong, and X. Liu: Simultaneous phase and size control of upconversion nanocrystals through lanthanide doping. *Nature* **463** (2010) 1061–1065. doi:10.1038/nature08777.

[37] Y. Tian, B. Yu, X. Li, and K. Li: Facile solvothermal synthesis of monodisperse Fe_3O_4 nanocrystals with precise size control of one nanometre as potential MRI contrast agents. *Journal of Materials Chemistry* **21** (2011) 2476–2481. doi:10.1039/c0jm02913k.

[38] B. Baruwati, M. N. Nadagouda, and R. S. Varma: Bulk Synthesis of Monodisperse Ferrite Nanoparticles at Water-Organic Interfaces under Conventional and Microwave Hydrothermal Treatment and Their Surface Functionalization. *Journal of Physical Chemistry C* **112** (2008) 18399–18404. doi:10.1021/jp807245g.

[39] R. De Palma, S. Peeters, M. J. Van Bael, H. Van den Rul, K. Bonroy, W. Laureyn, J. Mullens, G. Borghs, and G. Maes: Silane ligand exchange to make hydrophobic superparamagnetic nanoparticles water-dispersible. *Chemistry of Materials* **19** (2007) 1821–1831. doi:10.1021/cm0628000.

[40] C. Cannas, A. Musinu, A. Ardu, F. Orru, D. Peddis, M. Casu, R. Sanna, F. Angius, G. Diaz, and G. Piccaluga: $CoFe_2O_4$ and $CoFe_2O_4/SiO_2$ Core/Shell Nanoparticles: Magnetic and Spectroscopic Study. *Chemistry of Materials* **22** (2010) 3353–3361. doi:10.1021/cm903837g.

[41] Y. W. Jun, Y. M. Huh, J. S. Choi, J. H. Lee, H. T. Song, S. Kim, S. Yoon, K. S. Kim, J. S. Shin, J. S. Suh, and J. Cheon: Nanoscale size effect of magnetic nanocrystals and their utilization for cancer diagnosis via magnetic resonance imaging. *Journal of the American Chemical Society* **127** (2005) 5732–5733. doi:10.1021/ja0422155.

[42] B. P. Pichon, P. Louet, O. Felix, M. Drillon, S. Begin-Colin, and G. Decher: Magnetotunable Hybrid Films of Stratified Iron Oxide Nanoparticles Assembled by the Layer-by-Layer Technique. *Chemistry of Materials* **23** (2011) 3668–3675. doi:10.1021/cm201139s.

[43] C. Barrera, A. Herrera, Y. Zayas, and C. Rinaldi: Surface modification of magnetite nanoparticles for biomedical applications. *Journal of Magnetism and Magnetic Materials* **321** (2009) 1397–1399. doi:10.1016/j.jmmm.2009.02.046.

[44] A. Ruiz, Y. Hernandez, C. Cabal, E. Gonzalez, S. Veintemillas-Verdaguer, E. Martinez, and M. P. Morales: Biodistribution and pharmacokinetics of uniform magnetite nanoparticles chemically modified with polyethylene glycol. *Nanoscale* **5** (2013) 11400–11408. doi:10.1039/c3nr01412f.

[45] J. J. Olivero and R. L. Longbothum: Empirical fits to Voigt line-width – brief review. *Journal of Quantitative Spectroscopy & Radiative Transfer* **17** (1977) 233–236. doi:10.1016/0022-4073(77)90161-3.

[46] J. Humlíček: Optimized computation of the Voigt and complex probability functions. *Journal of Quantitative Spectroscopy & Radiative Transfer* **27** (1982) 437–444. doi:10.1016/0022-4073(82)90078-4.

[47] M. R. Bhat: Nuclear Data Sheets for A = 57. *Nuclear Data Sheets* **85** (1998) 415–536. doi:10.1006/ndsh.1998.0021.

[48] A. Murad and J. H. Johnston. Iron Oxides and Hydroxides. In *Mössbauer spectroscopy Applied to Inorganic Chemistry, vol. 2.* Plenum Press, New York (1987), pages 507–583.

[49] L. I. Schiff: *Quantum Mechanics.* McGraw-Hill, New York, 3rd edition, 1968.

[50] J. J. Sakurai: *Modern Quantum Mechanics.* Addison-Wesley, revised edition, 1994.

[51] D. A. Varshalovich, A. N. Moskalev, and V. K. Khersonskii: *Quantum Theory of Angular Momentum.* World Scientific, Singapore, 1988.

[52] W. Su, T. Zhang, L. Li, J. Xing, M. He, Y. Zhong, and Z. Li: Synthesis of small yolk-shell Fe_3O_4@TiO_2 nanoparticles with controllable thickness as recyclable photocatalysts. *RSC Advances* **4** (2014) 8901–8906. doi:10.1039/c3ra47461e.

[53] N. Ghows and M. H. Entezari: Sono-synthesis of core-shell nanocrystal (CdS/TiO_2) without surfactant. *Ultrasonics Sonochemistry* **19** (2012) 1070–1078. doi:10.1016/j.ultsonch.2012.01.009.